



In Situ Real-Time Determination of SO₂ Photochemical Oxidation in Nanoscale Sea Salt Aerosols based on Dark-Field Microscopy

Xijie Xiong¹, Zhibo Xie^{1*}, XiuLi Wei¹, Douguo Zhang³, Jianguo Liu¹, Huaqiao Gui^{1,2*}

¹Key Laboratory of Environmental Optics and Technology, Anhui Institute of Optics and Fine Mechanics, Chinese Academy of Sciences, Hefei 230031, China

²Institute of Environment, Hefei Comprehensive National Science Center, Hefei 231299, China

³Institute of Photonics, Department of Optics and Optical Engineering, University of Science and Technology of China, Hefei, Anhui 230026, China

Correspondence to: Zhibo Xie (zbxie@aiofm.ac.cn) and Huaqiao Gui (hqgui@aiofm.ac.cn)

Abstract. Heterogeneous reaction processes of aerosols play an important role in air quality and climate change. However, the lack of in-situ measurements of single-nanoparticle reactions results in large uncertainties in modeling the nanoparticle reaction kinetics. The study introduces a method to quantify reaction rates of single-nanoparticles using hygroscopic growth factors (GFs) and the Zdanovskii-Stokes-Robinson (ZSR) rule. Planar waveguide dark-field microscopy was employed to monitor sodium chloride (NaCl) aerosol GFs under ultraviolet (UV) irradiation and SO₂ exposure in real time. The results revealed a first-order reaction rate constant of 0.6523 h⁻¹ for 100 nm NaCl aerosols. Moreover, the reaction rate constant exhibits a non-monotonic size dependence on particle diameter-increasing in the 50-200 nm range and decreasing for particle sizes larger than 200 nm. This reflects a competitive interplay between the surface curvature effect at small particle sizes and specific surface area effect at larger sizes, which is further validated by a combined analysis based on transition state theory and the double-film mass transfer approach. Subsequently, sodium octyl sulfate (SOS) was introduced to form binary NaCl-based nanoaerosols, where the organic coating content was systematically varied under constant surface curvature to modulate the specific surface area. An increase in organic volume fraction reduces the effective specific surface area and suppresses heterogeneous reaction rates, accompanied by a pronounced nonlinear transition from partial to complete coating. This further confirms the experimentally observed size-dependent nonlinearity in reaction rates and offers new insights into nanoscale sulfate formation, improving atmospheric chemical models and pollution-climate assessments.

1 Introduction

Aerosol-atmosphere interactions are central to Earth's climate system and air quality (Carslaw et al., 2010; Li et al., 2024). Tropospheric aerosols not only scatter and absorb solar radiation but also serve as active media for multiphase oxidation reactions, which alter their chemical composition and physicochemical properties such as hygroscopicity and refractive index (Bi et al., 2013). These changes can significantly influence atmospheric visibility, cloud and fog formation, and wet



30 deposition processes (Cui et al., 2016; Persad et al., 2023). Under ambient sunlight, aerosols are exposed to oxidants such as ozone (O_3), hydroxyl radicals ($\cdot OH$), and reactive chlorine species (ClO_x) (Ma et al., 2010; Shang et al., 2021). These heterogeneous reactions drive compositional and morphological changes that modify optical and hygroscopic properties, enhance secondary pollutant formation, and regulate atmospheric oxidative capacity (Laskin et al., 2012; Keene et al., 1998; Rossi et al., 2003; Cao et al., 2023; Cao et al., 2024; Jing et al., 2023). Nanometer-sized aerosols, with high specific surface area, strong reactivity, and long-range transport potential, play a disproportionate role in atmospheric chemistry and climate 35 feedbacks. Notably, surface-catalyzed oxidation of S(IV) by Mn(III) at droplet interfaces can proceed two to three orders of magnitude faster than bulk-phase reactions, and neglecting such interfacial processes in models may substantially underestimate aerosol aging and cloud condensation nuclei (CCN) activity. These observations highlight the need for kinetic descriptions that incorporate particle-size and interface effects (Rosati et al., 2021; Wang et al., 2021; Gen et al., 2020; Liu et 40 al., 2021; Yang et al., 2023).

Traditional characterization of heterogeneous reaction kinetics is typically performed using laboratory-based flow reactors or smog chambers (Liu et al., 2020). For instance, the sulfate formation rate from the aqueous oxidation of SO_2 (or H_2O_2) can be determined offline after a given reaction time in an aerosol flow reactor, yielding kinetic parameters that represent the ensemble-averaged behavior of the aerosol population during the reaction process. To investigate the kinetics of individual 45 suspended micrometer-sized aerosol particles, Aerosol Optical Tweezers (AOT) have been developed (Angle et al., 2021). When combined with cavity-enhanced Raman spectroscopy, this technique enables the direct measurement of the kinetics of Fe(III)-catalyzed SO_2 heterogeneous oxidation within micrometer-sized droplets. The Raman signal, which reflects the temporal evolution of ionic strength, can be quantitatively correlated with reaction rates. This approach has been applied to elucidate mechanisms of sulfate formation via transition-metal-catalyzed oxidation on sea-salt aerosol surfaces and to 50 explore the influence of environmental factors on such interfacial processes. However, the determination of reaction kinetics for single nanometer-sized aerosol particles still remains challenging at present (Xie et al., 2023). A photonic-chip-based dark-field imaging technique has recently been reported for the *in situ* observation of nanoscale aerosols, enabling stable detection of particles as small as 50 nm across centimeter-scale fields of view. Individual particles deposited on the substrate can be monitored continuously for hours to days, while an integrated reaction chamber permits precise control of gas 55 composition, humidity, and temperature. This approach facilitates direct measurements of nanoscale heterogeneous reaction kinetics and their dependence on particle properties such as specific surface area and curvature, overcoming both the diffraction limitations of conventional optical methods and the incompatibility of electron microscopy with dynamic atmospheric environments (Kuai et al., 2019; Kuai et al., 2020; Xie et al., 2020).

Sea-salt aerosols constitute the largest mass fraction of natural atmospheric aerosols, and the contribution of nanometer-sized 60 particles during atmospheric transport is non-negligible (Chi et al., 2015; Gong et al., 2023). Their major component, sodium chloride, undergoes chemical transformation during transport from marine to continental regions under clear-sky conditions. Chloride ions released from sea-salt particles can form a series of reactive chlorine compounds (Su et al., 2022; Rossi et al., 2003), which significantly enhance the oxidative capacity of the atmosphere and promote the formation of secondary



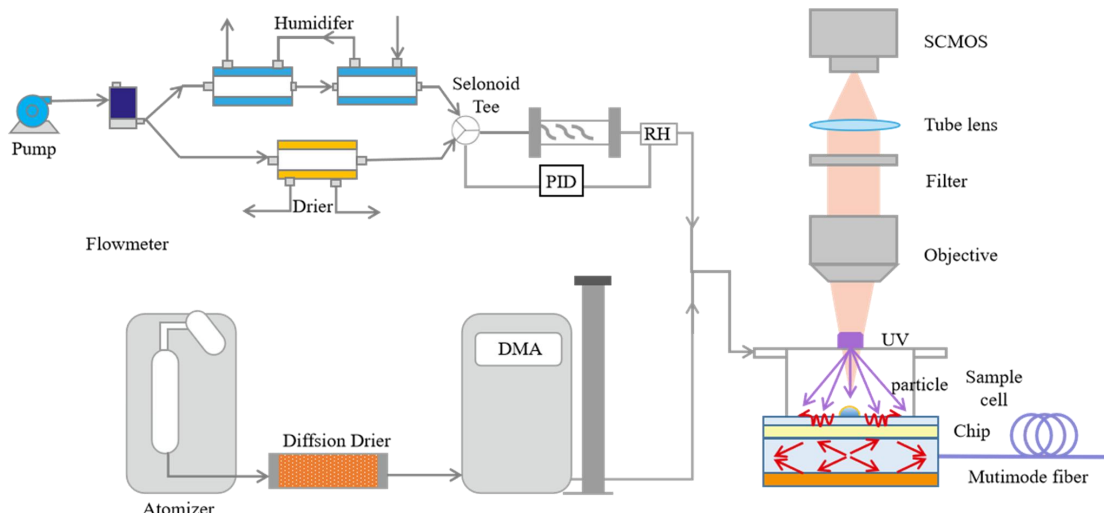
65 pollutants such as sulfate and nitrate (Wang et al., 2019; Zhang et al., 2021; Soni et al., 2023). Sea-salt particles frequently coexist with organic species to form mixed organic–inorganic aerosols, which often exhibit nonideal phase behavior such as liquid-liquid phase separation (LLPS) (Freedman et al., 2017; Zhang et al., 2022; Freedman et al., 2020). The formation of an organic shell can hinder the diffusion of reactive gases (e.g., HNO_3 , SO_2) into the inorganic core, thereby strongly affecting the kinetics of heterogeneous reactions.

70 In this study, we quantify the reaction rate of SO_2 photooxidation on nanoscale sea-salt aerosol droplets under UV irradiation by combining hygroscopic GF with the ZSR mixing rule. The GFs were obtained in real time using planar-waveguide dark-field microscopy under controlled UV and SO_2 exposure. By resolving the size-dependent kinetics in the 50–400 nm regime, we elucidate how nanoscale curvature and specific surface area jointly regulate heterogeneous reactivity, thereby providing quantitative constraints on the contribution of ultrafine sea-salt aerosols to the atmospheric sulfur cycle. In addition, by simulating surface modification through organic sulfonate coatings, we assess how reduced equivalent specific surface area 75 suppresses reaction rates, offering direct experimental evidence for sulfate formation pathways in complex atmospheric systems, including marine-organic mixtures and anthropogenically influenced aerosols. Collectively, these findings provide new insight into the mechanisms driving rapid sulfate production during haze episodes and improve our ability to predict how anthropogenic surfactant emissions may indirectly alter atmospheric chemistry by modifying aerosol surface reactivity.

2 Methods

80 2.1 Sample Preparation

The chemical reagent NaCl used for preparing nanoscale particulate aerosol particles was purchased from Sinopharm Chemical Reagent Co., Ltd. (Shanghai, China). A standard solution with a concentration of 1.0 g/L was prepared using ultrapure water from a Millipore Direct-Q3 system (Merck, Darmstadt, Germany). The standard solution was aerosolized into ultrafine aerosol particles with a particle size of approximately 50–400 nm using an aerosol generation system, which 85 consists of a MetOne 255 nebulizer, a silica gel diffusion dryer (to achieve a final relative humidity (RH) of <5 %), a TSI 3081 differential mobility analyzer, and a TSI 3080 platform (as shown in Figure 1). Monodisperse particles collided and deposited on the substrate surface in the sample chamber for 20 minutes. Mixed NaCl-(SOS) particles were generated from NaCl-SOS solutions with a prescribed mass ratio of 38:1, 18:1, 8:1, 4:1, 2:1 and 1:1 (OVF5 %, 10 %, 18 %, 33 %, 50 %, and 70 %).



90

Figure 1. Schematic diagram of the system for generation, aging, and hygroscopic growth measurements based dark-field imaging for single nanoparticles.

2.2 Sample Humidification and Aging

The RH was controlled using a humidifier, a dryer, and a proportional-integral-derivative (PID) controller, as shown in 95 Figure 1. The PID controller fed back a pulse signal to a three-way solenoid valve based on the desired and measured RH. The required RH was achieved by mixing dry and wet gases. During the photo-aging process, the sample underwent heterogeneous reactions with SO_2 . The reaction gases, nitrogen (N_2 , Qingjie Chemical Trading Co., Hefei, China) and sulfur dioxide (SO_2 , containing ppm levels of SO_2 in nitrogen; Qingjie Chemical Trading Co., Hefei, China), were supplied by gas cylinders, with flow rates controlled by mass flow meters to provide the desired SO_2 concentration. The gas containing the 100 desired SO_2 concentration was mixed with the gas at the required RH using a mixer, as shown in Figure 2.1, and then passed into the sample chamber containing the deposited particles. An RH of 85 % was selected to ensure that NaCl particles remained in an aqueous state and to facilitate efficient mass transfer and photochemical oxidation under humid conditions relevant to polluted environments (Rosati et al., 2021). An SO_2 concentration of 200 ppm, although higher than typical atmospheric background levels, was adopted to simulate extreme pollution scenarios (e.g., industrial plumes or severe 105 pollution events) and to provide sufficient signal for robust single-particle kinetic analysis within the experimental time scale (Yang et al., 2023). A UV light source was placed above the sample chamber (365–370 nm, 5 W) for effective simulation of daytime atmospheric photochemical processes. After the set reaction time, dry gas was injected into the sample chamber for 110 10 minutes to dry the particles, after which their hygroscopicity was measured. The reaction-rate calculation method used in this work was validated by ion chromatography (IC). Particles produced from the pure NaCl solution described in Sect. 2.1 were collected on quartz fiber filters (81 mm; TE-20-3010Z, Tisch Environmental) using a particle sampler, and



subsequently aged under the same conditions. After aging, the filters were cut into small pieces and extracted in ultrapure water. The concentrations of anions formed during aging were quantified by IC using a Dionex ICS-3000 system (Thermo Fisher Scientific). NaCl-SOS mixed particles were subjected to a humidification–drying cycle to induce LLPS, following the procedure reported by Zhang et al (Zhang et al.,2022). After LLPS formation, the mixed particles were aged under SO₂ 115 concentrations and UV irradiation intensities identical to those used for pure NaCl. For each OVF, particles were exposed to reaction times of 2 h and 3 h, respectively.

2.3 Measurement System

The measurement system illustrated in Fig. 2.1 is based on a photonic-chip-enabled evanescent-wave illumination scheme combined with dark-field optical imaging, which allows *in situ* characterization of individual aerosol nanoparticles down to 120 the nanometer scale. The photonic chip consists of a three-layer architecture designed to selectively manipulate the propagation and scattering of incident light. The middle layer is a ~2 μm thick dielectric film embedded with ~60 nm titanium dioxide (TiO₂) nanoparticles, which act as efficient scattering centers. The top and bottom layers are dielectric multilayer stacks composed of alternating silica (SiO₂) and silicon nitride (SiN_x) films, engineered to exhibit distinct photonic band gaps (PBGs). The optical reflectance of both multilayer stacks was calculated using the transfer matrix 125 method, as detailed in Kuai et al. (2020). For the bottom multilayer, a reflection minimum occurs near normal incidence for both transverse electric (TE) and transverse magnetic (TM) polarized light, such that only light propagating close to 0° can be transmitted at the design wavelength of 750 nm. Upon entering the TiO₂-doped scattering layer, the transmitted light undergoes multiple scattering events, resulting in a redistribution of propagation directions. Scattered light incident on the 130 bottom multilayer outside the narrow transmission window is reflected back into the scattering layer by the PBG, while only near-normal components are allowed to exit. The top multilayer is designed with a PBG centered at 750 nm, permitting transmission only for scattered light within a limited angular range. Scattered light with propagation directions exceeding a numerical aperture (NA) of 0.7 is reflected back into the scattering layer. Consequently, when an objective lens with NA < 0.7 is used, background illumination is effectively suppressed, enabling dark-field imaging. For illumination at 640 nm, the 135 scattered light lies within the photonic band gap of the multilayer structure; when the scattering angle exceeds the critical angle, evanescent waves are generated at the multilayer–air interface. Aerosol particles deposited on the surface of the top multilayer are selectively illuminated by these evanescent waves, producing high-contrast images with minimal background interference. This optical configuration enables sensitive detection of individual aerosol nanoparticles and allows continuous monitoring of their hygroscopic growth under controlled environmental conditions. During hygroscopicity measurements, 140 surface-wave images are recorded at each prescribed relative humidity (RH). The grayscale intensity of individual particles is extracted through image analysis, and the cube root of the normalized intensity is used to derive the hygroscopic growth factor (GF), as validated in Kuai et al. (2020). Importantly, the compact photonic-chip platform can be readily integrated with a series of upstream reaction chambers, enabling sequential exposure of the same individual particles to dynamically



controlled environments, including changes in RH, gas-phase composition, and irradiation conditions. This configuration allows real-time, single-particle tracking of physicochemical transformations in aerosol nanoparticles during hygroscopic 145 growth, phase transitions, and heterogeneous or photochemical reactions, providing a unique capability for simulating complex atmospheric processes under well-defined and time-resolved conditions

$$\frac{\sqrt[3]{Gray_{wet}}}{\sqrt[3]{Gray_{dry}}} = \frac{D_{wet}}{D_{dry}} = GF \quad (1)$$

where $Gray_{wet}$ and $Gray_{dry}$ represent the gray signal intensity of the surface wave image of the nanoparticles before and after humidification, and D_{dry} and D_{wet} represent the particle sizes before and after humidification.

150 2.4 Cocalulation of Reaction Rate

Based on the ZSR volume-weighted mixing rule, it is assumed that the components in the mixed particles retain their independent hygroscopic properties (Zangmeister et al., 2000). The hygroscopic GF of the mixed-component nanoparticles can be expressed as:

$$GF_{mixed} = (\sum_i^n \varepsilon_i GF_i^3)^{1/3} \quad (2)$$

$$155 \quad \varepsilon_i = \frac{w_i / \rho_i}{\sum_k^n w_k / \rho_k} \quad (3)$$

where GF_i is the hygroscopic growth factor of the pure component i , ε_i is the volume fraction of the pure component i in the dry state, w_k and ρ_k are the mass fraction and density of the pure component i , respectively, and n is the number of pure components.

Treat the reaction as a transformation of the particle from its initial compositional distribution to a final compositional 160 distribution (components that no longer change over time), for the conditions where no consecutive reactions occur, the particle after the reaction time t can be decomposed into a weighted mixture of the initial components and the final components:

$$GF_t = (\varepsilon_0 GF_0^3 + \varepsilon_T GF_T^3)^{1/3} \quad (4)$$

$$\varepsilon_0 + \varepsilon_T = 1 \quad (5)$$

165 Where GF_0 , GF_t , GF_T is the hygroscopic GF at the begining, time t and the end of the reaction, and t is the reaction time, T represents the time at which the reaction process of the individual nanoparticle reaches its limit under the reaction conditions. ε_0 , ε_t , are the dry volume fractions of the initial and final components after the reaction time t , respectively. By combining equations (3) and (4) can obtain:

$$\varepsilon_0 = \frac{GF_T^3 - GF_t^3}{GF_0^3 - GF_T^3} \quad (6)$$

170 In equation (2.6), the ratio of the initial component and final component in the intermediate state of the nanoparticle after the reaction time t is represented by ε_0 and $1-\varepsilon_0$, which allows the description of the progress of the reaction. For pure component nanoparticles, the initial component corresponds to the reactant, which is pure NaCl for NaCl particles. By combining



properties such as the density and molar mass, the concentration of the reactant or product over time can be calculated, ultimately enabling accurate inversion of the reaction rate.

175 For reactant, the concentration after the reaction time t can be calculated using the following formula:

$$C_t = \frac{\varepsilon_t V_t \rho}{M V_{t,RH}} = \frac{\rho \varepsilon_0}{M G F_{t,RH}^3} \quad (7)$$

$$C_0 = \frac{V_0 \rho}{M V_{0,RH}} = \frac{\rho}{M G F_{0,RH}^3} \quad (8)$$

where C_t , C_0 represents the concentration of the reactant at the initial and t -time during the reaction in the mixed particle under relative humidity RH. V_0 , V_t , $V_{0,RH}$, $V_{t,RH}$ is the dry volume of the mixed particle at the initial and t -time during the reaction, volume of the mixed particle at the initial and t -time during the reaction under relative humidity RH and $G F_{0,RH}$, $G F_{t,RH}$ is the hygroscopic GF at the initial and t -time during the reaction under relative humidity RH. ρ , M are the density and molar mass of the reactant, respectively.

By describe the concentration of the reactants or products over time, the slope of the tangent of the concentration-time curve of the component represents the instantaneous reaction rate. For reactions with specific relationships between concentration and time, a fitting function can be selected. For example, in the case of a first-order reaction, the concentration-time relationship is exponential, and the logarithmic plot of concentration versus time will yield a straight line, with the slope corresponding to the reaction rate constant. This slope represents the reciprocal of the time constant (the time at which the concentration of the original component decays to 1/e of its initial value).

2.5 Control of Biphase Droplet Phase State

190 To study the effect of droplet surface area on the reaction rate, we introduced SOS to cover the surface of the droplets. Therefore, we selected six OVF values (5 %, 10 %, 18 %, 33 %, 50 %, and 70 %) for the experiments to investigate the impact of a decrease in the specific surface area of nano-droplets on the gas-liquid reaction rate when the interface curvature is constant. This also provides a method for determining the phase state of nano biphase droplets. Six OVF values for the 195 binary particles were tested after 2 h and 3 h reaction times. The results were used to calculate the hygroscopic GF of the components of the binary particle, excluding SOS. Furthermore, the hygroscopic growth curves for NaCl and NaHSO₄ were obtained using the E-AIM model, based on Köhler theory.

3 Results and Discussion

3.1 Reaction Rate Measurement

3.1.1 Hygroscopic Growth Factor Measurement

200 NaCl particles were exposed to 85 % RH and UV irradiation, allowing it to undergo photochemical aging reactions with SO₂ gas. The aerosol was then dried, followed by humidification from 25 % RH to 85 % RH under reaction times of 1 h, 2 h, 3 h,



4 h, and 5 h. The results are shown in Figure 2, each data point represents the average value of GF measured for single particles at three randomly selected positions, with the standard deviation shown as error bars. As shown in Figure 2, the hygroscopicity of NaCl particles in response to SO₂ absorption exhibited different behaviors under low RH (<78 % RH) and 205 high RH (>78 % RH).

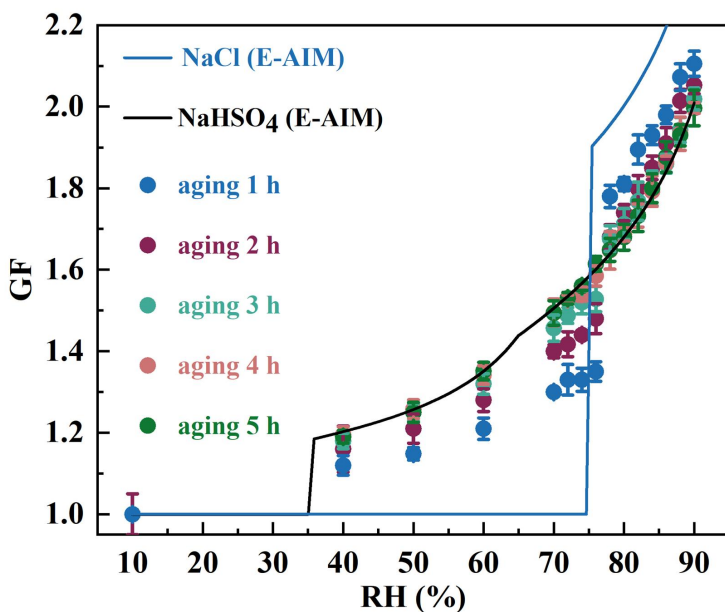


Figure 2. GFs of 100 nm NaCl particles after reaction times of 1 h, 2 h, 3 h, 4 h, and 5 h, together with the predicted GFs of NaCl and NaHSO₄.

When RH was less than 78 % RH (the deliquescence relative humidity (DRH) of NaCl), the reaction caused an increase in 210 the hygroscopicity of NaCl particles. As shown in Figure 2, compared to fresh NaCl particles (represented by red curve), the reaction products generally exhibited hygroscopicity at RH values below 78 %, with the increase in hygroscopicity becoming more pronounced with longer reaction times. After 4 hours of reaction, the hygroscopicity of the aerosols began to stabilize. When RH exceeded 78 % RH, the reaction caused a decrease in the hygroscopicity of NaCl aerosols. The hygroscopicity of the aged particle decreased at RH values above 78 %, and the reduction in hygroscopicity became more 215 pronounced with longer reaction times. Similar to the low RH scenario, the hygroscopicity began to stabilize after 4 hours of reaction.

The product of the oxidation reaction between NaCl and SO₂ could be Na₂SO₄ or NaHSO₄ (Wang et al., 2018), but the former is a substance with a higher DRH and stronger hygroscopicity upon deliquescence compared to NaCl, which is inconsistent with the measurements in this work. To determine the nature of the reaction products, we used the E-AIM



220 model to predict the hygroscopic curve of NaHSO_4 , which is shown by the black curve in Figure 2. This was compared with the GF measurements of the aged particle, and the predicted hygroscopic curve of NaCl . It can be seen that, at the same RH, the GF measurements of the aged aerosol moved towards the NaHSO_4 curve with increasing reaction time, moving away from the NaCl curve, and ultimately stabilizing near the NaHSO_4 curve. Based on this, we conclude that the reaction product is NaHSO_4 .

225 In conclusion, under 85 % RH and UV light conditions, NaCl aerosols absorb SO_2 and produce NaHSO_4 . The DRH of NaHSO_4 is 35 %, which allows the aged aerosol to exhibit hygroscopicity at low RH. At high RH, NaHSO_4 exhibits lower hygroscopicity than deliquescent NaCl , leading to a decrease in the hygroscopicity of aged aerosols at high RH. The longer the reaction time, the more NaHSO_4 is formed, resulting in stronger hygroscopicity at low RH and weaker hygroscopicity at high RH in the aged aerosols.

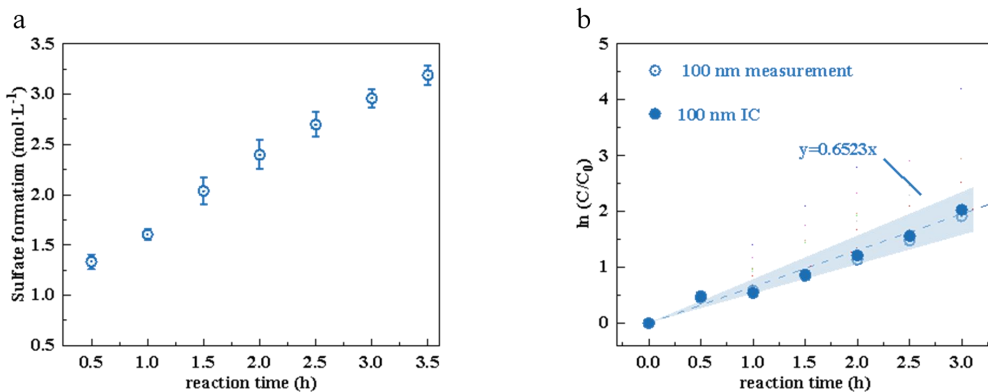
230 We observed that the evolution of aerosol hygroscopicity slowed with increasing reaction time. Compared to fresh NaCl aerosols, the GF of aged aerosols at 60 % RH increased by 14 %, 23 %, 30 %, 34 %, and 35 % after reaction times of 1 h, 2 h, 3 h, 4 h, and 5 h, respectively. After 4 hours of reaction, the GF showed little further increase. At 80 % RH, the GF decreased by 7.5 %, 11.4 %, 14.9 %, 15.9 %, and 16.4 % after reaction times of 1 h, 2 h, 3 h, 4 h, and 5 h, respectively, and after 4 hours of reaction, the GF showed little further decrease. This indicates that ultraviolet-catalyzed SO_2 uptake and 235 sulfate formation in NaCl particles are time-dependent, with the reaction rate decreasing as the reaction proceeds.

3.1.2 Reaction Rate Constant Calculation

We calculated the sulfate formation ($\text{mol}\cdot\text{L}^{-1}$) for droplets formed by 100 nm NaCl dry particles at fixed relative humidity (85 %RH) and SO_2 concentration (200 ppm) after different reaction times. The calculation results are shown in Figure 3a. Each data point represents the mean sulfate formation derived from single-particle GF measurements conducted at six 240 different RHs, with the corresponding standard deviations shown as error bars. Sulfate formation increased monotonically with reaction time, exhibiting a rapid increase during the initial stage followed by a gradual deceleration as the reaction progressed. After approximately 4 h, sulfate formation approached a plateau, suggesting that the reaction was nearing completion. The temporal evolution of sulfate formation is well described by an exponential function, indicating kinetically limited behavior. Consistent with this observation, the residual NaCl content within the droplet was quantified and plotted as 245 $\ln(C/C_0)$ versus reaction time (Figure 3b). As NaCl serves as the reactant, its concentration decreased exponentially with increasing reaction time. In the logarithmic space, $\ln(C/C_0)$ exhibited a linear dependence on time, yielding a slope of 0.6523, with the shaded region representing the 95 % confidence interval of the fitted curve. This behavior is consistent with a pseudo-first-order reaction with respect to NaCl , corresponding to an apparent rate constant of approximately 0.6523 h^{-1} . 250 independent validation was obtained from IC, which also plotted as $\ln(C_0/C)$ versus time. The IC-derived data show a consistent linear trend, corroborating the GF-based analysis and confirming the concurrent formation of sulfate and the



consumption of NaCl. This demonstrates that the combination of GF measurements and the ZSR mixing rule provides a reliable approach for inferring reaction kinetics in aerosol nanoparticles.



255 **Figure 3. (a) Sulfate concentration and (b) $\ln(C_0/C)$ of 100 nm NaCl droplets formed at 80 % RH as a function of reaction time. The inverse of the fitted slope k in the $\ln(C_0/C)$ - t plot represents the reaction time required for the NaCl concentration to decay to 1/e. The shaded region indicates the 95 % confidence interval of the linear fit..**

3.2 Size Dependence of Reaction Rates

From a kinetic perspective, bulk-phase reactions at constant RH are expected to exhibit size-independent reaction rates, whereas surface reactions should scale inversely with particle radius ($1/r$). To examine the role of particle size, sulfate formation was monitored as a function of time for NaCl particles with diameters ranging from 50 to 400 nm under UV-induced oxidation of SO₂ at 85 % RH. The temporal evolution of sulfate formation and the corresponding $\ln(C/C_0)$ values of residual NaCl for different particle sizes are shown in the Figure 4. Each data point in Figure 4a and b represents the average value of sulfate formation calculated from single-particle GF measurements conducted at six different RHs, with standard deviations represented as error bars. The shadow in Figure 4c and d represents the 95 % confidence interval of the fitted curve. Overall, sulfate formation and NaCl consumption exhibit similar kinetic behaviors to those observed for the 100 nm particles. For a given reaction time, the sulfate formation depends on particle size, reaching a maximum for particles with a diameter of approximately 200 nm. Sulfate production increased with particle size in the range of 50–200 nm, whereas a decreasing trend was observed for particles between 200 and 400 nm. Consistent with these observations, the $\ln(C/C_0)$ plots of NaCl residuals display size-dependent slopes, indicating that the apparent rate constants k varies with particle size. The highest k value was obtained for the 200 nm particles, revealing a non-monotonic dependence of reaction kinetics on particle size: k increased with particle size for particles smaller than 200 nm, but decreased for larger particles.

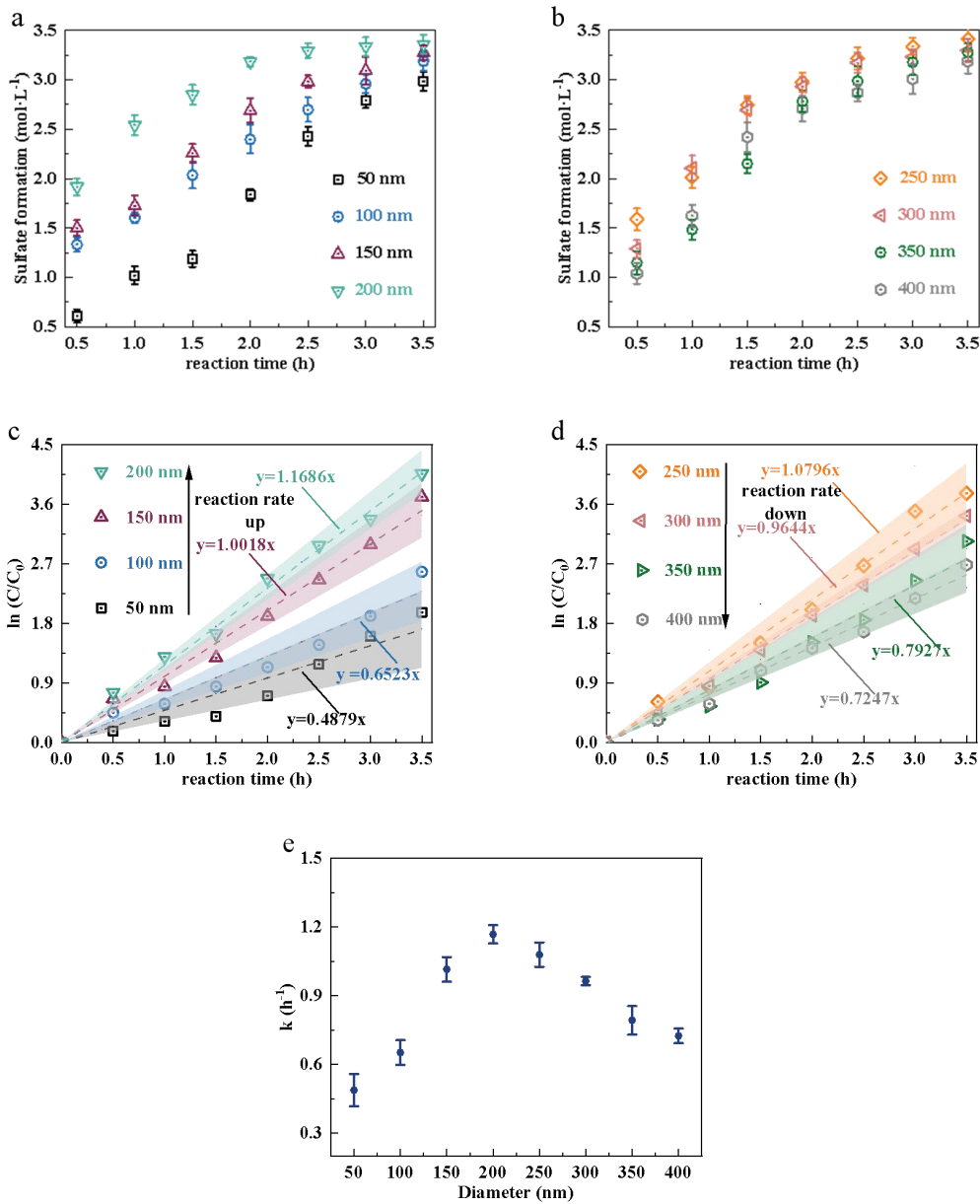




Figure 4. (a-b) Sulfate concentration and (c-d) $\ln(C_0/C)$ of 50 – 400 nm NaCl droplets formed at 80 % RH under different reaction times. The inverse of the fitted slope k in the $\ln(C_0/C)-t$ plot corresponds to the reaction time when 275 the NaCl concentration decays to 1/e. The shaded region represents the 95 % confidence interval of the fit.(e)relationship between k and dry diameters of particles.

The observed non-monotonic dependence of sulfate formation kinetics on particle size reflects the coexistence of distinct 280 kinetic regimes across the nano- to microscale. For nanoscale NaCl aerosols, the heterogeneous photochemical oxidation of SO_2 is governed primarily by interfacial and near-surface transport processes, whereas for larger droplets, surface-area limitations and bulk-phase diffusion progressively dominate the reaction kinetics. For particles with diameters between 50 and 200 nm, the apparent reaction rate increases with particle size. This behavior can be attributed to curvature-related 285 effects that suppress gas uptake and interfacial transport in very small droplets. According to Köhler theory, the increasing of the equilibrium vapour pressure above a curved droplet surface caused by decreasing radius due to the Kelvin effect renders net condensation and uptake thermodynamically less favorable for very small droplets (Kaku et al., 2006; Davies et al., 2019). In parallel, experimental and modeling studies have shown that the mass-accommodation (or uptake) coefficient decreases with increasing surface curvature, leading to reduced gas-to-particle fluxes for nanometer-sized droplets (Barclay et al., 2019). Kinetic multilayer models demonstrate that reduced accommodation or weakened surface driving forces directly translate into lower heterogeneous reaction rates when interfacial or near-surface transport becomes limiting (Shiraiwa et al., 2010; Chan, 2005). As a result, smaller particles (e.g., 50 and 100 nm) require longer equilibration times, 290 consistent with the reduced sulfate formation rates in this size range. As particle size increases toward 200 nm, the influence of curvature diminishes, facilitating more efficient gas uptake and enhancing the apparent reaction rate.

To rationalize the experimentally observed non-monotonic size dependence of the apparent reaction rate constant, we 295 develop a mechanistic framework that integrates transition state theory with a two-film-type resistance model. This approach enables a quantitative assessment of how curvature-modified interfacial reactivity and finite transport limitations jointly give rise to an optimal particle size. Following transition state theory, the probability (or rate coefficient) for gas–surface uptake can be written as an activated process,

$$\alpha \propto \exp\left(-\frac{\Delta G^\ddagger}{RT}\right)$$

Where ΔG^\ddagger is the activation free energy associated with interfacial adsorption or incorporation. For a curved interface, classical interfacial thermodynamics predicts that the interfacial free energy acquires curvature-dependent corrections. In the weak-curvature limit ($r \gg$ molecular length), the free energy can be expanded as

$$\Delta G^\ddagger(r) = \Delta G_\infty + \frac{C}{r}$$

300 consistent with Tolman-type curvature corrections and Helfrich curvature elasticity (Tolman et al., 1949; Capovilla et al., 2002). Substituting this expression into the activated uptake formulation yields



$$\alpha(r) \propto \exp\left(-\frac{\Delta G^\ddagger(\infty)}{k_B T}\right) \exp\left(-\frac{C}{k_B T r}\right) \propto \alpha(\infty) \exp\left(-\frac{r_c}{r}\right)$$

Where r_c is a characteristic curvature length scale determined by interfacial tension and molecular restructuring at the interface.

In addition to curvature-modified interfacial reactivity, the overall uptake rate is further constrained by geometric and transport limitations. Following a two-film-type resistance framework, the finite surface-area availability (scaling with particle radius r) and a finite effective reaction-diffusion depth δ can be treated as independent limitations acting in series (Guo et al., 2022). Here, δ represents an effective length scale that integrates near-surface diffusion, interfacial accommodation kinetics, and molecular restructuring within the condensed phase. These constraints can be combined into an effective length scale $r+\delta$, analogous to a Padé-type interpolation between surface-area-limited and transport-limited regimes.

310 Accordingly, the apparent heterogeneous rate constant can be approximated as

$$k \propto \frac{1}{r+\delta} \exp\left(-\frac{r_c}{r}\right)$$

This formulation recovers the correct limiting behaviors: for $r \gg \delta$, $k_{app} \sim 1/r$, consistent with surface-area control, whereas for $r \gg \delta$, the rate becomes insensitive to further size reduction due to transport and interfacial limitations. Differentiation of the above expression yields an optimal particle radius,

$$r_{opt} = \frac{r_c}{2} (1 + \sqrt{1 + 4\delta/r_c})$$

315 at which the enhancement from increasing surface area is balanced by curvature- and transport-induced suppression. An order-of-magnitude estimate for δ can be obtained by considering the diffusion of sulfate ions away from the interfacial reaction zone. The characteristic diffusion length is given by $\delta \sim (Dt)^{1/2}$, D is the effective diffusion coefficient of sulfate in concentrated NaCl solution and τ is the characteristic time over which surface-generated sulfate contributes to the measured concentration increase. Under the experimental conditions, δ is expected to be significantly reduced relative to dilute aqueous solutions due to high ionic strength and ion-ion interactions, yielding values on the order of 10^{-10} – 10^{-11} m²s⁻¹. For 320 reaction times of several seconds to tens of seconds, this results in diffusion lengths of approximately 100–300 nm. Using physically reasonable values of r_c (20–40 nm), consistent with curvature effects reported for inorganic and organic aerosol interfaces (Barclay et al., 2019), and δ (100–300 nm), representing effective mass-transfer and interfacial restructuring lengths, the predicted maximum in k_{app} occurs in the range of approximately 150–250 nm. This prediction is in excellent agreement with the experimentally observed transition in the apparent reaction rate constant.

325 Table 1 compares the kinetic data obtained in this study with those reported by Jing et al. (2023) and Zhang et al. (2023). For micrometer-sized NaCl droplets, such as those investigated by Jing et al. (2023) and Zhang et al. (2023), heterogeneous SO₂ oxidation proceeds predominantly under bulk-phase or diffusion-limited conditions. In this size regime, reactant concentrations remain sufficiently high during the early stages of the reaction, resulting in nearly constant reaction rates over time. In contrast, nanoscale droplets exhibit rapid reactant consumption and reach quasi-equilibrium on much shorter 330 timescales, leading to a pronounced temporal evolution of reaction kinetics.



Although direct quantitative comparison between nano- and microscale systems is complicated by differences in surface area, diffusion length, and SO_2 exposure conditions, the substantially higher sulfate concentrations formed in submicrometer droplets within 1 h highlight the enhanced reactivity of nanoscale aerosols. Under the kinetic framework proposed here, the sulfate concentration produced in 400 nm droplets after 1 h corresponds to that achieved in micrometer-sized droplets only 335 after substantially longer reaction times, underscoring the critical role of particle size in governing heterogeneous oxidation rates.

Table 1. Sulfate formation rates from heterogeneous oxidation of SO_2 in droplets of different sizes

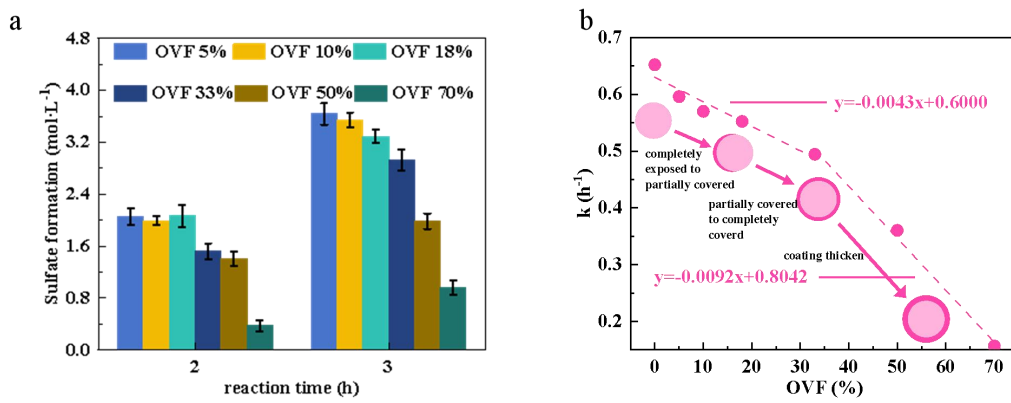
Reference	Medium	Catalyst	Conditions	Size	Sulfate formation of 1h ($10^{-3}\text{mol}\cdot\text{L}^{-1}$)
Zhang et al.(2023)	NaCl	UV	6.5 ppm SO_2 ; PH=7; 80% RH	57 \pm 2 μm	4.68
Jing et al.(2023)	NaCl	Mn(II)	1 ppm SO_2 ; PH=5~8; 80% RH	50 μm	36
				27 μm	43.5
				20 μm	54
				15 μm	72
				10 μm	108
				5 μm	216
The present study	NaCl	UV	200 ppm SO_2 ; PH=7; 80% RH	400 nm	1420
				300 nm	1841
				200 nm	2224
				100 nm	1404
				50 nm	894

3.3 Influence of Aerosol Mixing State on Reaction Rates

340 The effect of increasing particle size on the reaction rate discussed above reflects the combined influence of surface-to-volume ratio and surface curvature. To qualitatively assess the role of surface-area-related limitations independent of curvature effects, a series of controlled experiments employing organic surface coatings was conducted. This approach aims does not strictly decouple geometric and interfacial effects, but provides a proxy for evaluating how reductions in effective reactive surface area influence reaction kinetics under otherwise comparable conditions. SOS was selected as the additive, 345 representing organic sulfonates that constitute an important fraction of SOA, accounting for approximately 5–30 % of the



total organic aerosol mass (Zhang et al., 2022). These compounds contain hydrophilic sulfate groups and exhibit surface activity. When mixed with inorganic salts, they can induce LLPS, which modifies the hygroscopicity, scattering properties, and material exchange between aerosols and the atmosphere (Zhang et al., 2022; Freedman et al., 2020). GF measurements were performed for binary NaCl-SOS particles following UV-induced SO_2 oxidation over different reaction times. Sulfate formation and the corresponding NaCl residuals expressed as $\ln(C/C_0)$ were subsequently derived (Figure 5a and b), the shaded regime in Figure 5b represents the 95 % confidence interval of the fitted curve.



355 **Figure 5 (a) Sulfate concentration of NaCl-SOS mixed particles with different OVF after reaction times of 2 h and 3 h, and (b) the corresponding reaction rate constants k . The shaded areas denote the 95 % confidence intervals of the linear fits.**

The GF measurements of the binary particles are shown in Table S2. Binary particles consistently exhibited lower sulfate formation at a given reaction time compared to monodisperse NaCl particles with the same NaCl mass (Figure 5a). In logarithmic kinetic space, this behavior corresponds to smaller slope of $\ln(C/C_0)$ versus time. The magnitude of this difference increases with increasing OVF, suggesting that the presence of the organic phase inhibits the heterogeneous reaction between NaCl and SO_2 .

360 This inhibition is consistent with the formation of an organic coating on the surface of NaCl particle surface via LLPS, which introduces an additional barrier between the aqueous and gas phases. Importantly, the introduction of the organic phase alters not only the exposed reactive surface area but also the interfacial transport properties. Consequently, the observed kinetic suppression should be interpreted as the combined effect of reduced effective surface area and hindered interfacial transport. Nevertheless, the OVF-dependent trends provide insight into the relative importance of surface-area-related limitations. The samples tested, with an effective surface-to-volume ratio comparable to or greater than 100 nm monodisperse aerosols, exhibit a slower sulfate formation rate, confirming that an increase in surface-to-volume ratio is unfavorable for mass transfer. As the OVF increases from 0 %, the coverage of the NaCl droplet surface by the SOS layer



expands reduces the fraction of exposed inorganic surface while leaving the particle curvature essentially unchanged. In this
370 sense, the experiments approximate a scenario in which the effective reactive surface-area-to-volume ratio decreases without invoking curvature-related effects. In the low-OVF regime (OVF < 33 %), whereas a more pronounced decrease in k is observed at higher OVF (Figure 5b). This behavior is consistent with a transition from partial to more extensive surface coverage, although the exact coverage state cannot be uniquely determined from the present data. When compared with the particle-size-dependent trends observed for monodisperse NaCl aerosols, these results suggest that a reduction in effective
375 surface-area-to-volume ratio alone leads to a decrease in the heterogeneous reaction rate. This contrasts with the increasing reaction rate observed for small monodisperse particles in the 50–200 nm size range, where reduced surface curvature is expected to facilitate gas uptake and interfacial transport. Taken together, these findings support the interpretation that curvature-related effects dominate the enhancement of reaction rates in the small-particle regime, whereas surface-area-related limitations become increasingly important once curvature effects are minimized.

380 4 Conclusion

In this work, we measured the UV catalyzed SO_2 conversion in nanometer-sized sea-salt aerosol droplets and confirmed that hygroscopic measurements based on dark-field optical microscopy, combined with the ZSR model, can be utilized in inverting the heterogeneous reaction rate of single nanoparticles. We found that, at the nanoscale, the UV-catalyzed SO_2 oxidation in aerosol droplets follows a first-order reaction. In the small particle size range (<200 nm), an increase in particle
385 size positively influences the reaction rate, which is likely attributable to the inhibitory effect of increased surface curvature on the mass transfer rate. However, for particles larger than 200 nm, the decrease in surface-to-volume ratio limits mass transfer efficiency, and the reaction rate becomes negatively correlated with particle size. This suggests that the UV-catalyzed oxidation of sea-salt aerosols in the atmosphere exhibits a pronounced particle-size dependence, whereby particles within specific size ranges dominate sulfate production through this pathway relative to other size fractions. When
390 nonreactive material forms a core-shell structure, the liquid outer layer can mask surface-active sites and effectively reduce the available specific surface area, thereby limiting mass transport and substantially suppressing the sulfate formation rate. Collectively, these findings provide new insights into the mechanisms driving the rapid formation of nanoscale sulfate components during haze episodes and enhance our ability to predict how organic aerosols may indirectly influence atmospheric chemistry by altering the aerosol surface properties.

395

Acknowledgement

This work was Supported by the National Natural Science Foundation of China (42305143, 42375124), the Science and Technological Fund of Anhui Province (grant nos. 2308085QD128), the Research Team Construction Project of Hefei Comprehensive Science Center Environmental Research Institute (HYKYTD2024006).



400 **References**

Angle, K. J., Neal, E. E., and Grassian, V. H.: Enhanced Rates of Transition-Metal-Ion-Catalyzed Oxidation of S(IV) in Aqueous Aerosols: Insights into Sulfate Aerosol Formation in the Atmosphere, *Environ. Sci. Technol.*, 55, 10291–10299, <https://doi.org/10.1021/acs.est.1c01932>, 2021.

Barclay, P. L., and Lukes, J. R.: Curvature dependence of the mass accommodation coefficient, *Langmuir*, 35, 6196–6262, <https://doi.org/10.1021/acs.langmuir.9b00537>, 2019.

Bi, J., Huang, J., Hu, Z., Holben, B. N., and Guo, Z.: Investigating the aerosol optical and radiative characteristics of heavy haze episodes in beijing during january of 2013, *J. Geophys. Res. Atmos.*, 119, 9884-9900, <https://doi.org/10.1002/2014JD021757>, 2013.

Cao, X., Chen, Z., Liu, Y., Jing, X., Li, L., Liu, P., and Zhang, Y.: Directly Measuring Fe(III)-catalyzed SO₂ Oxidation Rate in Single Optically Levitated Droplets, *Environ. Sci. Atmos.*, 3, 298-304, <https://doi.org/10.1039/d2ea00125j>, 2023.

Cao, X., Liu, Y., Huang, Q., Chen, Z., Sun, J., Sun, J., Pang, S., Liu, P., Wang, W., Zhang, Y., Ge, M.: Single Droplet Tweezer Revealing the Reaction Mechanism of Mn(II)-Catalyzed SO₂ Oxidation, *Environ. Sci. Technol.*, 58, 5068–5078, <https://doi.org/10.1021/acs.est.4c00309>, 2024.

Capovilla, R., Guven, J., and Santiago, J. A.: Lipid membranes with an edge, *Phys. Rev. E*, 66, 021607, <https://doi.org/10.1103/PhysRevE.66.021607>, 2002.

Carslaw, K. S., Boucher, O., Spracklen, D. V., Mann, G. W., Rae, J. G. L., Woodward, S., and Kulmala, M.: A review of natural aerosol interactions and feedbacks, *Atmos. Chem. Phys.*, 10, 1701–1737, <https://doi.org/10.5194/acp-10-1701-2010>, 2010.

Chan, M. and Chan, C.: Mass transfer effects in hygroscopic measurements of aerosol particles, *Atmos. Chem. Phys.*, 5, 2703-2712, <https://doi.org/10.5194/acp-5-2703-2005>, 2005.

Chi, J., Li, W., Zhang, D., Zhang, J., Lin, Y., Shen, X., Sun, J., Chen, J., Zhang, X., Zhang, Y., and Wang, W.: Sea salt aerosols as a reactive surface for inorganic and organic chemistry, *Atmos. Chem. Phys.*, 15, 11341–11361, <https://doi.org/10.5194/acp-15-11341-2015>, 2015.

Cui, X., Wang, X., Yang, L., Chen, B., Chen, J., Andersson, A., and Gustafsson, Ö.: Radiative absorption enhancement from coatings on black carbon aerosols, *Sci. Total Environ.*, 551, 51-56, <https://doi.org/10.1016/j.scitotenv.2016.02.026>, 2016.

Davies, J. F., Zuend, A., and Wilson, K. R.: Technical note: The role of evolving surface tension in the formation of cloud droplets, *Atmos. Chem. Phys.*, 19, 2933–2946, <https://doi.org/10.5194/acp-19-2933-2019>, 2019.

Finlayson-Pitts, B. J., and Hemminger, J. C.: Physical chemistry of airborne sea salt particles and their components, *J. Phys. Chem. A.*, 104, 11463–11477, <https://doi.org/10.1021/jp002968n>, 2000.

Freedman, M. K.: Liquid–Liquid Phase Separation in Supermicrometer and Submicrometer Aerosol Particles, *Acc. Chem. Res.*, 53, 1102–1110, <https://doi.org/10.1021/acs.accounts.0c00093>, 2020.



Freedman, M. K.: Phase Separation in Organic Aerosol, *Chem. Soc. Rev.*, 46, 7694, <https://doi.org/10.1039/c6cs00783j>, 2017.

Gen, M., Zhang, R., Li, Y., and Chan, C.: Multiphase Photochemistry of Iron-Chloride Containing Particles as a Source of
435 Aqueous Chlorine Radicals and Its Effect on Sulfate Production, *Environ. Sci. Technol.*, 54, 9862–9871,
<https://doi.org/10.1021/acs.est.0c01540>, 2020.

Gupta, D., Kim, H., Park, G., Li, X., Eom, H. J., and Ro, C. U.: Hygroscopic properties of NaCl and NaNO₃ mixture
particles as reacted inorganic sea-salt aerosol surrogates, *Atmos. Chem. Phys.*, 15, 3379–3392,
<https://doi.org/10.5194/acp-15-3379-2015>, 2015.

440 Gong, X., Zhang, J., Croft, B., Yang, X., Frey, M., Bergner, N., Chang, R. Y., Creamean, J. M., Kuang, C. A., Martin, R. V.,
Ranjithkumar, A., Sedlacek, A. J., Uin, J., Willmes, S., Zawadowicz, M. A., Pierce, J. R., Shupe, M.D., Schmale, J., Wang,
J.: Arctic warming by abundant fine sea salt aerosols from blowing snow, *Nat. Geosci.*, 16, 768–774,
<https://doi.org/10.1038/s41561-023-01254-8>, 2023.

445 Jing, X., Chen, Z., Cao, X., Huang, Q., Liu, P., and Zhang, Y.: Rapid Sulfate Formation via Mn²⁺-Catalyzed SO₂ Oxidation
on the Surface of NaCl Microdroplets, *J. Phys. Chem. C.*, 127, 13632–13638, <https://doi.org/10.1021/acs.jpcc.3c02839>,
2023.

Kaku, K. C., Hegg, D. A., Covert, D. S., Santarpia, J. L., Jonsson, H., Buzorius, G., and Collins, D. R.: Organics in the
Northeastern Pacific and their impacts on aerosol hygroscopicity in the subsaturated and supersaturated regimes, *Atmos.
Chem. Phys.*, 6, 4101–4115, <https://doi.org/10.5194/acp-6-4101-2006>, 2006.

450 Keene, W. C., Sander, R., Pszenny, A. A. P., Vogt, R., Crutzen, P. J., and Galloway, J. N.: Aerosol pH in the marine
boundary layer: A review and model evaluation, *J. Aerosol Sci.*, 29, 339–356, [https://doi.org/10.1016/s0021-8502\(97\)10011-8](https://doi.org/10.1016/s0021-
8502(97)10011-8), 1998.

Kuai, Y., Chen, J., Tang, X., Xiang, Y., Lu, F., Kuang, C., Xu, L., Shen, W., Cheng, J., Gui, H., Zou, G., Wang, P., Ming, H.,
Liu, J., Liu, X., Lakowicz, J. R., and Zhang, D. G.: Label-free surface-sensitive photonic microscopy with high spatial
455 resolution using azimuthal rotation illumination, *Sci. Adv.*, 5, eaav5335, <https://doi.org/10.1126/sciadv.aav5335>, 2019.

Kuai, Y., Xie, Z., Chen, J., Gui, H., Xu, L., Kuang, C., Wang, P., Liu, X., Liu, J., Lakowicz, J. R., and Zhang, D. G.: Real-
Time Measurement of the Hygroscopic Growth Dynamics of Single Aerosol Nanoparticles with Bloch Surface Wave
Microscopy, *ACS Nano.*, 14, 9136–9144, <https://doi.org/10.1021/acsnano.0c04513>, 2020.

460 Laskin, A., Moffet, R., Gilles, M., Fast, J., Zaveri, R., Wang, B., Nigge, P., and Shutthanandan, J.: Tropospheric chemistry
of internally mixed sea salt and organic particles: Surprising reactivity of NaCl with weak organic acids, *J. Geophys. Res.
Atmos.*, 117: D15302, <https://doi.org/10.1029/2012JD017743>, 2012.

Li, G., Su, H., Li, M., Kuhn, U., Zheng, G., Han, L., Bao, F., Pöschl, U., Cheng, Y.: Reactive uptake coefficients for
multiphase reactions determined by a dynamic chamber system, *Atmos. Meas. Tech.*, 15, 6433–6446,
<https://doi.org/10.5194/amt-15-6433-2022>, 2022.



465 Li, L., Liu, P., Huang, Q., Zhang, X., Chao, X., Pang, S., Wang, W., Cheng, Y., Su, H., Zhang, Y., and Ge, M.: Rethinking urban haze formation: Atmospheric sulfite conversion rate scales with aerosol surface area, not volume, *One Earth*, 7, 1082–1095, <https://doi.org/10.1016/j.oneear.2024.05.007>, 2024.

Liu, T., and Abbatt, J. P. D.: Oxidation of sulfur dioxide by nitrogen dioxide accelerated at the interface of deliquesced aerosol particles, *Nat. Chem.*, 13, 1173–1177, <https://doi.org/10.1038/s41557-021-00777-0>, 2021.

470 Liu, T., Clegg, S. L., and Abbatt, J. P. D.: Fast oxidation of sulfur dioxide by hydrogen peroxide in deliquesced aerosol particles, *Proc. Natl. Acad. Sci. U. S. A.*, 117, 1354–1359, <https://doi.org/10.1073/pnas.1916401117>, 2020.

Ma, J., Chen, Y., Wang, W., Yan, P., Liu, H., Yang, S., Hu, Z., Lelieveld, J.: Strong air pollution causes widespread haze-clouds over China, *J. Geophys. Res. Atmos.*, 115, D18204, <https://doi.org/10.1029/2009JD013065>, 2010.

Murphy, D. M., Froyd, K. D., Bian, H. S., Brock, C. A., Dibb, J. E., DiGangi, J. P., Diskin, G., Dollner, M., Kupc, A., 475 Scheuer, E. M., Schill, G. P., Weinzierl, B., Williamson, C., and Yu, P.: The distribution of sea-salt aerosol in the global troposphere, *Atmos. Chem. Phys.*, 19, 4093–4104, <https://doi.org/10.5194/acp-19-4093-2019>, 2019.

Persad, G. G.: The dependence of aerosols' global and local precipitation response on emission location and cloud regime, *Atmos. Chem. Phys.*, 23, 3435–3456, <https://doi.org/10.5194/acp-23-3435-2023>, 2023.

Rosati, B., Christiansen, S., Dinesen, A., Roldin, P., Massling, A., Nilsson, E.D., and Bilde, M.: The impact of atmospheric 480 oxidation on hygroscopicity and cloud droplet activation of inorganic sea spray aerosol, *Sci. Rep.*, 11, 10008, <https://doi.org/10.1038/s41598-021-89346-6>, 2021.

Rossi, M. J.: Heterogeneous reactions on salts, *Chem. Rev.*, 103, 4823–4882, <https://doi.org/10.1021/cr020507n>, 2003.

Shang, D., Peng, J., Guo, S., Wu, Z., and Hu, M.: Secondary aerosol formation in winter haze over the Beijing-Tianjin-Hebei Region, China, *Front. Environ. Sci. Eng.*, 15, 1–13, <https://doi.org/10.1007/s11783-020-1326-x>, 2021.

485 Shiraiwa, M., Pfrang, C., and Pöschl, U.: Kinetic multi-layer model of aerosol surface and bulk chemistry (KM-SUB): Model formulation and application to heterogeneous oxidation of oleic acid, *Atmos. Chem. Phys.*, 10, 3673–3691, <https://doi.org/10.5194/acp-10-3673-2010>, 2010.

Soni, M., Sander, R., Sahu, L. K., Taraborrelli, D., Liu, P., Patel, A., Girach, I. A., Pozzer, A., Gunthe, S. S., and Ojha, N.: 490 Comprehensive multiphase chlorine chemistry in the box model CAABA/MECCA: implications for atmospheric oxidative capacity, *Atmos. Chem. Phys.*, 23, 15165–15190, <https://doi.org/10.5194/acp-23-15165-2023>, 2023.

Su, B., Wang, T., Zhang, G., Liang, Y., Lv, C., Hu, Y., Li, L., Zhou, Z.: Wang, X.M., and Bi, X.H.: A review of atmospheric aging of sea spray aerosols: Potential factor affecting chloride depletion, *Atmos. Environ.*, 290, 119365, <https://doi.org/10.1016/j.atmosenv.2022.119365>, 2022.

Tolman, R. C.: The effect of droplet size on surface tension, *J. Chem. Phys.*, 17, 333–337, <https://doi.org/10.1063/1.1747247>, 495 1949.

Wang, W., Liu, M., Wang, T., Song, Y., Zhou, L., Cao, J., Hu, J., Tang, G., Chen, Z., Li, Z., Xu, Z., Peng, C., Lian, C., Chen, Y., Pan, Y., Zhang, Y., Sun, Y., Li, W., Zhu, T., Tian, H., and Ge, M.: Sulfate Formation is Dominated by



ManganeseCatalyzed Oxidation of SO₂ on Aerosol Surfaces During Haze Events, *Nat. Commun.*, 12, 1993, <https://doi.org/10.1038/s41467-021-22091-6>, 2021.

500 Wang, X., Jacob, D., Eastham, S., Sulprizio, , Zhu, L., Chen, Q., Alexander, B., Sherwen, T., Evans, M. J., Lee, B. H., Haskins, J. D., Lopez-Hilfiker, F. D., Thornton, J. A., Huey, G.L., and Liao, H.: The role of chlorine in global tropospheric chemistry, *Atmos. Chem. Phys.*, 19, 3981–4008, <https://doi.org/10.5194/acp-19-3981-2019>, 2019.

Wang, Z., Jing, B., Shi, X., Tong, S., Wang, W., and Ge, M.: Importance of water-soluble organic acid on the hygroscopicity of nitrate, *Atmos. Environ.*, 190, 65-73, <https://doi.org/10.1016/j.atmosenv.2018.07.010>, 2018.

505 Xie, Z., Gui H., Zhang, J., Yang, B., Kang, S., Wei, X., Yu T., Yang, Y., Liu, J., Liu, W.: Measurement techniques new progress of atmospheric fine particles, *Energy Environ. Prot.*, 37, 16-29, <https://doi.org/10.20078/j.eep.20230308>, 2023.

Xie, Z., Kuai, Y., Liu, J., Gui, H., Zhang, J., Dai, H., Xiao, H., Chen, D., and Zhang, D.: In situ quantitative observation of hygroscopic growth of single nanoparticle aerosol by surface plasmon resonance microscopy, *Anal. Chem.*, 92, 11062-11071, <https://doi.org/10.1021/acs.analchem.0c00431>, 2020.

510 Yang, B., Xie, Z., Liu, J., Gui, H., Zhang, J., Wei, X., Wang, J., Fan, Z., and Zhang, D.: Investigating the hygroscopicities of calcium and magnesium salt particles aged with SO₂ using surface plasmon resonance microscopy, *Sci. Total Environ.*, 867, 161588, <https://doi.org/10.1016/j.scitotenv.2023.161588>, 2023.

Zangmeister, C., and Pemberton, J.: Raman Spectroscopy and Atomic Force Microscopy of the Reaction of Sulfuric Acid with Sodium Chloride, *J. Am. Chem. Soc.*, 122, 12289-12296, <https://doi.org/10.1021/ja001469x>, 2000.

515 Zhang, H., Xu, Y., and Jia, L.: A chamber study of catalytic oxidation of SO₂ by Mn²⁺/Fe³⁺ in aerosol water, *Atmos. Environ.*, 245, 118019, [http://doi.org/10.1016/j.atmosenv.2020.118019](https://doi.org/10.1016/j.atmosenv.2020.118019), 2021.

Zhang, J., Wang, Y., Teng, X., Liu, L., Xu, Y., Ren, L., Shi, Z., Zhang, Y., Jiang, J., Liu, D., Hu, M., Shao, L., Chen, J., Martin, S., Zhang, X., and Li, W.: Liquid-liquid Phase Separation Reduces Radiative Absorption by Aged Black Carbon Aerosols, *Comun. Earth Environ.*, 3, 128, <https://doi.org/10.1038/s43247-022-00462-1>, 2022.

520 Zhang, R., and Chan, C.: Simultaneous formation of sulfate and nitrate via co-uptake of SO₂ and NO₂ by aqueous NaCl droplets: combined effect of nitrate photolysis and chlorine chemistry, *Atmos. Chem. Phys.*, 23, 6113-6126, <https://doi.org/10.5194/acp-23-6113-2023>, 2023.